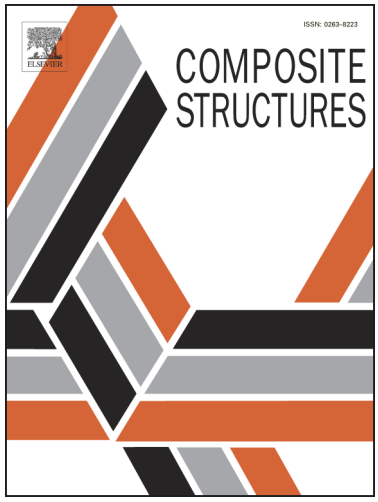

Nonlinear dynamic analysis of harmonically excited debonded sandwich plates using finite element modelling

V.N. Burlayenko, T. Sadowski

PII: S0263-8223(13)00489-3
DOI: http://dx.doi.org/10.1016/j.compstruct.2013.09.042
Reference: COST 5374

To appear in: *Composite Structures*

Please cite this article as: Burlayenko, V.N., Sadowski, T., Nonlinear dynamic analysis of harmonically excited debonded sandwich plates using finite element modelling, *Composite Structures* (2013), doi: http://dx.doi.org/10.1016/j.compstruct.2013.09.042

Nonlinear dynamic analysis of harmonically excited debonded sandwich plates using finite element modelling

V.N. Burlayenko [a,b,*], T. Sadowski[a]

[a]*Department of Solid Mechanics, Lublin University of Technology, 40 Nadbystrzycka St., 20-618 Lublin, Poland*
[b]*Department of Applied Mathematics, National Technical University 'KhPI', 21 Frunze St., 61002 Kharkov, Ukraine*

Abstract

Nonlinear dynamic aspects of a rectangular simply supported sandwich plate with a central penny-shaped debonded zone subjected to harmonic loading have been studied by using the finite element analysis within the ABAQUS code. In order to accurately predict the response of the debonded sandwich plate to harmonic loading, contact-impact and sliding conditions along the damaged skin-to-core interface were imposed in the model via the penalty contact algorithm in the framework of an implicit integration scheme. The relevant qualitative parameters such as frequency response curves, phase portraits and Poincaré maps were extracted from time history signals calculated by the finite element analysis for sandwich plates with and without debonded region. The results of the both plates were compared, to specify the effects associated with the presence of debond on the forced vibrations of the sandwich plate. A wide range of forcing frequencies was applied to illustrate various nonlinear responses occurring in the debonded plate's dynamics. A considerable influence of contact events within the debonded region on the global dynamic response of the debonded plate was found out. The predictions performed also showed that the finite element model applied would be useful for nondestructive evaluation of defects in composite sandwich plates, and for studying dynamic response of such plates to periodic oscillations.

Keywords: sandwich plates, skin-to-core debond, nonlinear forced vibrations, dynamic contact, finite element analysis

1. Introduction

Over the past few decades sandwich panels have become a popular structural component in many industrial applications where dynamic loading prevails. The reason thereof is superior properties of sandwich structures over the conventional metallic counterparts. In general, a sandwich panel is a special type of laminates where a layer made of a more flexible and lightweight material (core) is located between two strength and stiff face sheets (skins). This structural concept provides high bending stiffness and strength of the sandwich structure without adding much weight [1]. However, the bonded interface between too dissimilar materials of the core and skins is the weakest point of such structures. Wrong manufacture processes or unfavorable service conditions can induce the appearance of a partially debonded region along the skin-to-core interface. Experimental observations [2] have shown that the presence of debond in sandwich panels affects their integrity and reduces their overall stiffness and strength and, as a consequence, alternates their dynamic responses. Therefore, in order to provide reliability and durability of sandwich structural elements in service, the modelling of dynamic behavior of sandwich panels with an existing debonded zone is highly required at the design stage.

The dynamic behavior of intact sandwich panels is the subject of extensive studies, e.g. [3–5] among many others. In contrast to this, papers reported on the dynamic behavior of sandwich panels with debond are less presented in the literature. Apart from the nonlinearities mentioned for the dynamics of perfectly bonded sandwich beams, plates and shells, the vibrations of those debonded structural elements are accompanied by additional types of nonlinear phenomena. Contact and impact, and friction between the detached surfaces of skin and core are main among others. Even assuming that the influence of nonlinearities others than contact-impact and friction are negligible, this is true for most of real structures vibrating at a forced frequency that is far from a resonance frequency, simulations of the dynamic behavior accounting for contact and friction are a challenging problem yet in the structural analysis.

One of the possibilities to tackle the dynamic contact-impact problem arising in cracked structures is the reducing of an underlying complex structure to a simple model with one or several number of degrees of freedom [6]. Such spring-mass-damper models were successful to reveal nonlinear responses of composite beams with interfacial damage such as sub- and superharmonic resonances, cascades of period doubling bifurcation and the existence of chaotic motion, e.g. it can be found in [7–10]. Additional studies of complex phenomena in vibro-impacting systems such as a grazing of periodic orbits, a period-adding sequence and the coexistence of different attractors for the same control parameters with complex basins of attraction can be found in many recent papers, e.g. [11–14]. While the oscillator models, used in those studies have shed some light on the nonlinear phenomena of cracked structures they suffer

*Corresponding author
Email addresses: burlayenko@yahoo.com (V.N. Burlayenko), t.sadowski@pollub.pl (T. Sadowski)

from the lack of information about a spatial presentation of both the deformation modes and distributions of interlaminar stresses within the cracked region. Thereby continuous models of vibrating structures damaged by cracks, explicitly describing the interaction between the detached segments, are still highly required.

Since a sandwich plate can be referred to a kind of laminate, the debonded zone within it can be treated as an equivalence to a delaminated region, hence, analytical, numerical and experimental approaches developed for studying dynamic delamination effects (see [15] for an overview) can be, in essence, adapted for the vibration analysis of debonded sandwich plates. The split spanwise region approach and the constrained model envisaging the same movement of separated segments for an across-the-width debonded region was used to find an analytical solution for the free vibration analysis of a debonded sandwich beam with anisotropic composite laminates skins and an orthotropic honeycomb core in [16]. The authors presented parametric studies of free vibrations depending on properties of face sheets, core and debonded zone geometry. In [17] a strip element method technique was utilized to simulate the propagation of wave fields in a sandwich plate containing non-bonded regions located symmetrically above and below the core. For the sake of simplicity, the problem was reduced to a two dimensional beam model and the debonded regions were modelled as a rectangular flaw spreading through the core thickness. The unconstrained debonding model which permits the overlap between the debonded surfaces of skins and core was adopted in that research. Based on this approach an analytical model was developed by Kim and Hwang in [18] to study effects of the symmetrically located debonds on reduction in the flexural bending stiffness and natural frequencies of honeycomb sandwich beams with laminated skins. The results obtained analytically were, then, compared with experimental observations. Recently, the same analytical formulation has been applied and verified through appropriate experiments to evaluate free vibration characteristics of sandwich beams with a single and two symmetrical debonds at the interface between the carbon fiber reinforced plastic (CFRP) face sheets and honeycomb core in [19]. A semi-analytical approach relying on the high order sandwich panel theory was developed in [20] for studying a transient dynamic response of a simply supported sandwich beam with a single debonded region. A set of nonlinear governing equations of motion of the debonded beam accounted for explicit contact conditions at the debonded interface without using contact mechanics formulations. The system of equations was numerically solved by using the Newmark-beta method for integration over time.

The versatility of the finite element method (FEM) for solving complex topological and multi-physical problems has made it a popular means in investigations of debonded sandwich panels. In [21] both the FEM analysis and experimental investigations were performed to obtain natural frequencies and a steady state response of a honeycomb sandwich plate with aluminum skins containing a circular debonded zone at the center. The developed three-dimensional FE model of the plate used a hexahedron element with eight nodes. The assumptions of free debonding model were accepted at the debonded region. Finite element predictions of vibration and buckling of laminated sandwich plates with skin-to-core interface layers damaged at different levels using a refined higher order shear deformation theory were performed in [22]. The interlaminar imperfection was modelled by a linear spring layer model implemented into an elaborated 6-node triangular finite element. Using the spring model definition, pointwise spring finite elements within a three-dimensional FE model applied for the free vibration analysis were introduced into a debonded region of a sandwich plate to avoid interpenetration between the detached face sheet and core in [23, 24]. This model allowed authors to evaluate the influence of debonded zones' size and form as well as their location and number on natural frequencies and mode shapes of sandwich plates with different core types and subjected to different boundary conditions. However, no contact interactions have been taken into account. Kwon and Lannamann in [25] have investigated transient dynamics of a debonded sandwich plate using a FE model where time dependent contact conditions at the damaged interface were simulated. A kinematic node-to-node frictionless contact algorithm was utilized. A much more sophisticated FE simulation of the contact-impact phenomenon taking place between thin detached part and remaining beam was carried out in [26]. To obtain correct numerical results in a stationary case of forced motion, authors applied the surface-to-surface penalty based frictionless contact algorithm with contact damping within the LS-DYNA code. A nonlinear dynamic analysis of sandwich plates containing a post-impact zone involving core fracture and interfacial debond under impulse and harmonic loads was done in [27]. In those simulations the surface-to-surface contact definition and kinematic contact algorithm within the ABAQUS code were used to model the contact phenomenon during forced oscillations. Although the global dynamic response of the sandwich plates was examined, the contact impact phenomenon existing between the detached skin and core was not investigated in detail in that paper. A detailed analysis and simulation of nonlinear dynamics of a simply supported rectangular sandwich plate with a penny-shaped debonded zone has been carried out using the ABAQUS/Explicit code in [28]. While this research provided a formulation based on the formalism of continuum mechanics of the underlying elastodynamic problem involving contact and friction laws, the numerical studies were there rather demonstrative examples than investigations on the nature of nonlinear forced dynamics.

Thereby, it follows from the literature search results that suitable three-dimensional models to simulate the dynamics of sandwich plates weakened by the partially damaged skin-to-core interface are still high required for investigating nonlinear effects occurring in them. In this article, a nonlinear dynamic behavior of simply supported rectangular sandwich plate with a central penny-shaped debonded zone subjected to harmonic excitations is studied. While the spatial discretization of the debonded sandwich plate is the same as in [28], an alternative solution technique is utilized within the ABAQUS code in the current work. In contrast to the explicit solution methodology used in [28], an implicit direct integration scheme exploiting

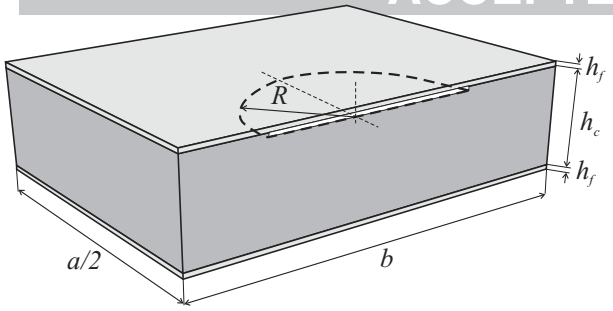

Figure 1: Half of sandwich plate with penny-shaped debonded zone.

the Hilbert-Hughes-Taylor operator with controllable numerical damping and the Newmark formulae is applied here. Also, the penalty method and the return mapping algorithm, which are consistent with the implicit time stepping scheme, are used for resolving local contact and friction problems, respectively. Based on this numerical algorithm, nonlinear features exhibited by the vibrating debonded sandwich plate are investigated in detail. To detect nonlinearities existing due to the "breathing" behavior of the debonded zone, response signals of both the debonded sandwich plate and the same intact plate predicted numerically are compared. The estimations of spectral components in time history signals as well as comparisons of phase orbits, frequency response curves and Poincaré sections are used to evaluate the nonlinearities appeared.

2. Finite element formulations

2.1. Elastodynamic contact problem

The object of our investigations is a rectangular sandwich plate containing a central penny-shaped zone of radius R between the upper skin and the core, as shown in Fig. 1. The plate is subjected to an external time-dependent load. In general, forced dynamics of the debonded sandwich plate is inherently nonlinear, even if small displacements and the simplest linear constitutive relations are presumed, because the contact problem between the detached skin and core. The introduction of friction between the contacting segments is another involved source of nonlinearity. As a result, an elastodynamic problem formulated for the debonded sandwich plate consists of a complete set of equations relating to the initial boundary-value problem with boundary conditions being a part of the solution. Mathematical aspects of a general elastodynamic contact problem are widely discussed and presented in enormous number of publications on contact mechanics. Thus, in the present paper only a brief formulation of this problem in the extent that is needed just for basic finite element procedures used is given below. For more details in this topic we refer to books on contact mechanics, e.g. [29, 30].

Considering the plate as a deformable body occupying a domain $\Omega \in \mathcal{R}^3$ at time $t \in [0, T]$ with a boundary $\Gamma \in \mathcal{R}^2$ such that $\Gamma_t \cup \Gamma_u = \Gamma$ and $\Gamma_t \cap \Gamma_u = \varnothing$, where Γ_t and Γ_u are parts of the boundary Γ with prescribed traction $\bar{\mathbf{t}}$ and displacements $\bar{\mathbf{u}}$, respectively, and containing an internal discontinuity on a boundary Γ_c (with an open set $\tilde{\Omega} = \Omega \setminus \Gamma_c$), we can formulate the elastodynamic contact problem in context of finite element approximations as follows:

For given the boundary conditions $\bar{\mathbf{t}}$ *on* Γ_t^h, $\bar{\mathbf{u}}$ *on* Γ_u^h, *the initial conditions* $\mathbf{u}_0$ *and* $\mathbf{v}_0$ *in* $\tilde{\Omega}^h$, *the distributed body forces* $\mathbf{b}$ *in* $\tilde{\Omega}^h$ *and the contact conditions on* Γ_c^h *find* $\mathbf{u}(t) \in U^h$ *for every time* $t \in [0, T]$ *such that for all admissible* $\delta\boldsymbol{u} \in U_0^h$

$$\int_{\tilde{\Omega}^h} \delta\mathbf{u} \cdot \rho\ddot{\mathbf{u}} d\Omega + \int_{\tilde{\Omega}^h} \delta\mathbf{u} \cdot c\dot{\mathbf{u}} d\Omega + \int_{\tilde{\Omega}^h} \{\delta\boldsymbol{\varepsilon} : \boldsymbol{\sigma} - \delta\mathbf{u} \cdot \rho\mathbf{b}\} d\Omega - \int_{\Gamma_t^h} \delta\mathbf{u} \cdot \bar{\mathbf{t}} d\Gamma + \int_{\Gamma_c^h} (t_N \delta g_N + \mathbf{t}_T \cdot \delta\mathbf{g}_T) d\Gamma = 0 \tag{1}$$

Here, all the quantities denoted by superscript (h) are finite-dimensional counterparts of the continuous ones. In doing so, the total discretized domain Ω^h is a union of element subdomains Ω_e, i.e. $\Omega^h = \bigcup_e \Omega_e$. As well, approximated displacement field $\mathbf{u}$ and its variations $\delta\mathbf{u}$ within each finite element Ω_e reside in the appropriate finite-dimensional vector spaces:

$$\begin{aligned} U^h &= \{\mathbf{u} | \mathbf{u} \in \mathcal{H}^1(\tilde{\Omega}^h), \mathbf{u} = \bar{\mathbf{u}} \text{ on } \Gamma_u^h, \text{ discontinuous on } \Gamma_c^h\} \\ U_0^h &= \{\delta\mathbf{u} | \delta\mathbf{u} \in \mathcal{H}^1(\tilde{\Omega}^h), \delta\mathbf{u} = 0 \text{ on } \Gamma_u^h \cup \Gamma_c^h\} \end{aligned} \tag{2}$$

Furthermore, in Eq. (1) it is denoted that ρ is the mass density, c is the linear viscous damping parameter representing the system material damping, $\boldsymbol{\sigma}$ and $\boldsymbol{\varepsilon}$ are discrete stress and strain fields, respectively. In order to focus only on nonlinearities resulting from intermittent contact in the debonded zone, the small strain tensor $\boldsymbol{\varepsilon} = \frac{1}{2}\left(\nabla\mathbf{u} + (\nabla\mathbf{u})^T\right)$ and a linear elastic material behavior defined by Hooke's law $\boldsymbol{\sigma} = \mathbb{C} : \boldsymbol{\varepsilon}$, where $\mathbb{C}$ is the fourth-order material tensor, are adopted in (1).

Integrands of the last integral in Eq. (1), so-called contact integral specify constraints that should be imposed on the current solution for displacements $\mathbf{u}$ and traction $\boldsymbol{\sigma}$ on the contact boundary Γ_c^h at an instant of time when contact is active. Since they deserve a special attention, their definitions are given in the next subsection.

2.2. Contact interface modelling

The kinematics of points on the contact boundary Γ_c^h, in terms of the "master-slave" contact definition commonly used in the finite element formulation, is defined by the gap functions g_N and $\mathbf{g}_T$ which describe relative movements between those points in normal and tangential directions, respectively. They can be presented in the forms [29]:

$$g_N = (\mathbf{x}^- - \bar{\mathbf{x}}^+) \cdot \bar{\mathbf{n}}^+ \tag{3}$$

and

$$\mathbf{g}_T = g_{T_\alpha} \bar{\mathbf{a}}^{+^\alpha} \quad \text{with} \quad g_{T_\alpha} = (\mathbf{x}^- - \bar{\mathbf{x}}^+) \cdot \bar{\mathbf{a}}_\alpha^+, \tag{4}$$

where $\mathbf{x}^-$ is a point of slave surface and $\bar{\mathbf{x}}^+(\bar{\xi}^1, \bar{\xi}^2)$ is its orthogonal projection on the master surface parameterized by ξ^α $(\alpha = 1, 2)$, and $\bar{\mathbf{n}}^+$ is the unit vector normal to the master surface and $\bar{\mathbf{a}}_\alpha$ $(\alpha = 1, 2)$ are the tangent base vectors at the point

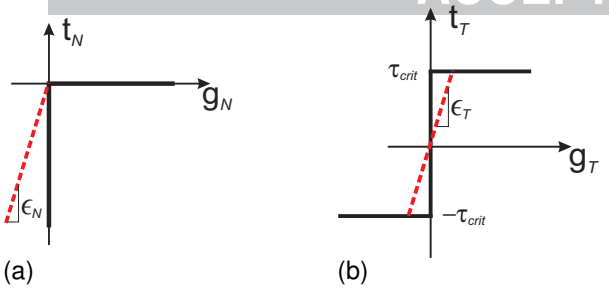

Figure 2: a) Normal contact conditions; and b) tangential contact conditions.

$\bar{\mathbf{x}}^+$. In the geometrically linear case, the rate of tangential gap function at this point can be found as

$$\dot{\mathbf{g}}_T = \dot{\xi}^\alpha \bar{\mathbf{a}}^+_\alpha = \dot{g}_{T_\alpha} \bar{\mathbf{a}}^{+^\alpha} \quad \text{with} \quad \dot{g}_{T_\alpha} = \left(\dot{\mathbf{x}}^- - \dot{\bar{\mathbf{x}}}^+\right) \cdot \bar{\mathbf{a}}^+_\alpha = a_{\alpha\beta} \dot{\xi}^\beta, \tag{5}$$

where $a_{\alpha\beta} = \bar{\mathbf{a}}^+_\alpha \cdot \bar{\mathbf{a}}^+_\beta$ is the metric tensor at $\bar{\mathbf{x}}^+$.

When contact on Γ^h_c happens, the contact traction $\mathbf{t}_c = \boldsymbol{\sigma} \cdot \mathbf{n}_c$ is transmitted over Γ^h_c, where $\mathbf{n}_c$ is an outward unit normal at a contact point. The vector $\mathbf{t}_c$ can be decomposed into normal $\mathbf{t}_N$ and tangential $\mathbf{t}_T$ components for each contact pair, i.e. $\mathbf{t}_c = \mathbf{t}_N + \mathbf{t}_T$. In turn, the contact traction components are conjugated to the normal g_N and tangential $\mathbf{g}_T$ gap functions, thus, relations between them specify the appropriate contact constraints on Γ^h_c.

The impenetrability constraints (Fig. 2a) can be formulated in the view of Karush-Kuhn-Tucker conditions as follows:

$$t_N \le 0, \quad g_N \ge 0 \quad \text{and} \quad t_N g_N = 0, \tag{6}$$

where t_N is the scalar quantity of the normal contact pressure, i.e. $\mathbf{t}_N = t_N \bar{\mathbf{n}}^+$.

The friction behavior arising due to tangential interactions has to fulfil the constraints (Fig. 2b) that can be stated in the form:

$$\|\mathbf{t}_T\| \le \tau_{crit}, \quad \|\mathbf{g}_T\| \ge 0, \quad (\|\mathbf{t}_T\| - \tau_{crit})\|\mathbf{g}_T\| = 0, \tag{7}$$

where τ_{crit} is a threshold of tangential contact traction when a tangential slip occurs. The value of threshold is evaluated according with a friction law adopted. Throughout this work we consider the Coulomb friction model that defines $\tau_{crit} = \mu t_N$, where μ is the coefficient of friction.

The using an analogy between plasticity and friction leads to the following form of (7):

$$\dot{\mathbf{g}}^{slip}_T = \dot{\gamma} \frac{\partial \Phi(\mathbf{t}_T)}{\partial \mathbf{t}_T} = \dot{\gamma} \frac{\mathbf{t}_T}{\|\mathbf{t}_T\|}, \tag{8}$$

along with loading-unloading conditions in the form:

$$\Phi \le 0, \quad \dot{\gamma} \ge 0 \quad \text{and} \quad \Phi \dot{\gamma} = 0, \tag{9}$$

where the potential function is presented by $\Phi(\mathbf{t}_T) = \|\mathbf{t}_T\| - \mu t_N$ with the Euclidean norm $\|\mathbf{t}_T\|^2 = a^{\alpha\beta} t_{T\alpha} t_{T\beta}$ as in [30].

2.3. Equations of motion with contact

Following the standard finite element procedure [31], assumed finite element approximations of displacements and their variations and material derivatives are substituted into the momentum equality (1). After the known manipulations with its terms, we can write down the spatially discretized finite element equations of motion for the elastodymamic contact problem in hand as follows:

$$\mathbf{M}\ddot{\mathbf{U}}(t) + \mathbf{C}\dot{\mathbf{U}}(t) + \mathbf{K}\mathbf{U}(t) = \mathbf{F}^{ext}(\mathbf{U}(t)) - \mathbf{F}^{cont}(\mathbf{U}(t)) \tag{10}$$

Herewith the system of nonlinear ordinary differential equations (10) is subjected to initial conditions on $\dot{\mathbf{U}}(0)$ and $\mathbf{U}(0)$, boundary conditions on Γ^h_u, and impenetrability (6) and friction (8) and (9) conditions on Γ^h_c.

In (10) at each instant of time t we define that $\ddot{\mathbf{U}}(t)$, $\dot{\mathbf{U}}(t)$ and $\mathbf{U}(t)$ are the global vectors of unknown accelerations, velocities and displacements, $\mathbf{F}^{ext}$ and $\mathbf{F}^{cont}$ are the global vectors of the given external and calculated contact forces, and $\mathbf{M}$, $\mathbf{C}$ and $\mathbf{K}$ are the global mass, damping and stiffness matrices, respectively. These global vectors and matrices are typically calculated by the assembly of element level contributions for each Ω_e. In doing so, the global contact force vector $\mathbf{F}^{cont}(\mathbf{U})$ is expressed as the assembly of contact elemental force contributions specified for a set of nodes, or points or elements in the contact interface Γ^h_c at a certain instant of time. Thus, the set of active contacts should be known before solving (10). For this purpose iterative processes referring to as the contact searching algorithms are applied, [29, 30]. As a result, the nearest neighbor segments potentially coming into contact and projections to the definitions of both g_N and $\mathbf{g}_T$ are being calculated.

Eq. (10) is nonlinear, because while there are neither geometrical nor material nonlinearities, the contact force vector derived from the contact integral in (1) is highly nonlinear by the definition. The actual expressions for the contact forces which are associated with the normal contact pressure and tangential traction, depend on the contact algorithm adopted. Among of most commonly used are the penalty method, Lagrange multiplier method, augmented Lagrangian constraint techniques and predictor/corrector kinematic algorithms, which must be consistent with a temporal integration scheme used for solving (10). On the other hand, the contact traction components are related to the appropriate gap functions, which in turn are functions of the approximated displacements and are computed depending on the contact formulation used on the discretized boundary Γ^h_c . In this respect either node-to-node or node-to-surface or surface-to-surface contact formulations can be utilized in conjunction with defined kinematic assumptions.

The system material damping defined by the matrix $\mathbf{C}$ in (10) is assumed that can be represented by Rayleigh damping:

$$\mathbf{C} = \alpha\mathbf{M} + \beta\mathbf{K} \tag{11}$$

The factors α and β can be determined on the basis of the modal damping ratio:

$$\xi_n = \frac{\alpha}{2\omega_n} + \frac{\beta\omega_n}{2}, \tag{12}$$

by specifying any desirable ratio for any two selected frequencies ω_n of the undamped system with the given $\mathbf{M}$ and $\mathbf{K}$.

2.4. Implicit time-stepping procedure

The semi-discrete system of equations (10) has to be completely discretized by applying an approximation in the time domain. Hence, the solution satisfying (10) can only be found in a finite number of time steps, i.e. $[0,T] \equiv \bigcup_{i=0}^{L-1}[t_i, t_{i+1}]$, where $t_i < t_{i+1}$, and $t_0 = 0$, $t_L = T$. Let the time increment be $\triangle t = t_{i+1} - t_i$ and accelerations, velocities and displacements referring to this time increment are denoted by $\ddot{\mathbf{U}}_{i+1}$, $\dot{\mathbf{U}}_{i+1}$ and $\mathbf{U}_{i+1}$, respectively. Then the totally discretized system of equations at a certain time t_{i+1} can be written down as follows:

$$\mathbf{M}\ddot{\mathbf{U}}_{i+1} + \mathbf{C}\dot{\mathbf{U}}_{i+1} + \mathbf{K}\mathbf{U}_{i+1} = \mathbf{F}^{ext}_{i+1} - \mathbf{F}^{cont}_{i+1}, \tag{13}$$

with the initial conditions $\mathbf{U}_0 = \bar{\mathbf{U}}$ and $\dot{\mathbf{U}}_0 = \bar{\mathbf{V}}$, given displacement boundary conditions and boundary conditions being calculated due to developing contact.

A temporal integration scheme should be utilized for finding the solution of the discrete equations (13). In this respect, either explicit or implicit integration schemes can be used. The explicit time-stepping algorithm based on the central difference operator is well suitable for using in simulations of fast dynamic transient analyses. However, this method is only conditionally stable and requires a very small time step and a large number of such steps for the solution. Therefore, for long-term dynamic analyses such as forced vibrations under harmonic loading, a huge number of such steps will be required, as a result, there will be a significant computational cost and roundoff errors resulting in even numerical blow-ups. Thus, to ensure robustness and stability of the calculations over long time scales, the use of an implicit integration technique is often more effective. In this study we consider the Hilber-Hughes-Taylor temporal integrator [32], which is the second order accurate, unconditionally stable with controllable numerical damping scheme. Moreover, this scheme inherits conservation linear and angular momenta by construction. Thereby, Eq. (13) is replaced by:

$$\begin{aligned}
\mathbf{M}\ddot{\mathbf{U}}_{i+1} + \mathbf{C}\dot{\mathbf{U}}_{i+\alpha_B} + \mathbf{K}\mathbf{U}_{i+\alpha_B} &= \mathbf{F}^{ext}(t_{i+\alpha_B}) - \mathbf{F}^{cont}(\mathbf{U}_{i+\alpha_B}) \\
\mathbf{U}_{i+\alpha_B} &= \alpha_B\mathbf{U}_{i+1} + (1-\alpha_B)\mathbf{U}_i \\
\mathbf{U}_{i+1} = \mathbf{U}_i + \triangle t_{i+1}\dot{\mathbf{U}}_i + \tfrac{\triangle t^2}{2}[(1-2\beta)\ddot{\mathbf{U}}_i + 2\beta\ddot{\mathbf{U}}_{i+1}] \\
\dot{\mathbf{U}}_{i+1} &= \dot{\mathbf{U}}_i + \triangle t[(1-\gamma)\ddot{\mathbf{U}}_i + \gamma\ddot{\mathbf{U}}_{i+1}]
\end{aligned} \tag{14}$$

where $\beta = \frac{1}{4}(1-\alpha_B)^2$, $\gamma = \frac{1}{2} - \alpha_B$ and $-\frac{1}{3} \leqslant \alpha_B \leqslant 0$, [33]. Control over the amount of numerical damping is provided by the parameter α_B.

The time integrator leads to a nonlinear algebraic problem which has to be solved at each time step. For this, the Newton-Raphson iterative method is employed. Hence, the linearized problem should be solved for each iteration indexed by n as follows:

$$\begin{aligned}
&\frac{\partial}{\partial \mathbf{U}}\left[\mathbf{M}\ddot{\mathbf{U}} + \mathbf{C}\dot{\mathbf{U}} + \mathbf{K}\mathbf{U} - \mathbf{F}^{cont}(\mathbf{U})\right]_{\mathbf{U}^n_{i+\alpha_B}} \triangle\mathbf{U} = \\
&\mathbf{F}^{ext}(t_{i+\alpha_B}) - \mathbf{M}\ddot{\mathbf{U}}^n_{i+1} - \mathbf{C}\dot{\mathbf{U}}^n_{i+\alpha_B} + \mathbf{K}\mathbf{U}^n_{i+\alpha_B} - \mathbf{F}^{cont}(\mathbf{U}^n_{i+\alpha_B})
\end{aligned} \tag{15}$$

with iterations updated by $\mathbf{U}^{n+1}_{i+1} = \mathbf{U}^n_{i+1} + \triangle\mathbf{U}$.

The system of equations (13) is accompanied by contact and friction constraints given on Γ^h_c, then, a local algorithm that is consistent with the global implicit time stepping scheme (14) should be applied to calculations of contact forces at each time step in (15). In this regard, the penalty parameter method and the Lagrange multiplier method can be used. Merits and drawbacks of both methods are theoretically well known and discussed extensively, e.g. in [29, 30]. It is well known that the Lagrange multiplier method introduces extra unknowns. Because of this, to retain the computational efficiency of ongoing predictions, the penalty contact approach is used for resolving contact problems in the current investigation.

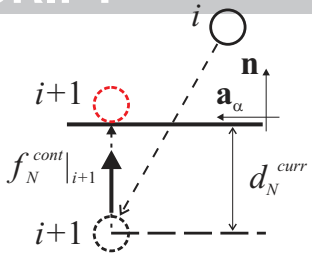

Figure 3: Penalty contact constraint algorithm.

In this framework, the normal contact pressure is proportional to the depth of penetration, i.e. $t_N = \epsilon_N H(g_N)$, where $H(\bullet)$ is the Heaviside function. The penalty parameter ϵ_N is determined so that a penetration is eliminated on the next configuration updated with the actual displacements at t_{i+1} (see Fig. 3). A penalty regularization of the frictional problem can be formulated with a tangential penalty parameter ϵ_T, i.e. $\mathbf{t}_T = \epsilon_T\mathbf{g}_T$. The regularized forms of these interfacial laws are displayed by the dotted lines in Figs. 2a and b, respectively.

On the consideration of sliding contact, since the frictional traction depends on the rate of the gap function (8) within the global time-stepping scheme (14), a local update algorithm for the current tangential traction $\mathbf{t}_{T\,i+1}$ is required. The implementation of the penalized friction law into the implicit HHT scheme used is accomplished by applying the trial/return map algorithm to (8) and (9) discretized with the backward Euler method [31]. The algorithm is doing the following. First, within the time step t_{i+1} both the normal gap $g_{N\,i+1}$ and the increment of the tangential gap $\triangle\mathbf{g}_{T\,i+1}$ is calculated based on the current kinematic state $\mathbf{U}_{i+1}$. Then, a trial state is defined as follows

$$\mathbf{t}^{trial}_{T\,i+1} = \mathbf{t}_{T\,i} + \epsilon_T\triangle\mathbf{g}_{T\,i+1} \tag{16}$$

The slip potential in terms of the trial traction is calculated as

$$\Phi^{trial}_{i+1} = \|\mathbf{t}^{trial}_{T\,i+1}\| - \mu t_{N\,i+1} \tag{17}$$

Thereafter, the slip condition is checked. If $\Phi^{trial}_{i+1} \leq 0$ no slip takes place, i.e. $\mathbf{t}_{T\,i+1} = \mathbf{t}^{trial}_{T\,i+1}$ and $\mathbf{g}_{T\,i+1} = \frac{1}{\epsilon_T}\mathbf{t}_{T\,i+1}$. In case of $\Phi^{trial}_{i+1} > 0$ the return mapping is performed as follows:

$$\begin{aligned}
\mathbf{t}_{T\,i+1} &= \mu t_{N\,i+1}\frac{\mathbf{t}^{trial}_{T\,i+1}}{\|\mathbf{t}^{trial}_{T\,i+1}\|} \\
\mathbf{g}_{T\,i+1} &= \mathbf{g}_{T\,i} + \frac{1}{\epsilon_T}\Phi^{trial}_{i+1}\frac{\mathbf{t}^{trial}_{T\,i+1}}{\|\mathbf{t}^{trial}_{T\,i+1}\|}
\end{aligned} \tag{18}$$

It is should be noted that in calculations of the contact stiffness arising from the linearized part of (15), linearization of the corresponding terms in the contact integral, consistent with the time stepping algorithm applied is performed. The the contact force vector in the right side of (15) is evaluated using the numerical integration in a finite number of quadrature points.

2.5. Finite element model

The finite element model used in simulations of dynamics of a simply supported rectangular sandwich plate with a circular debonded zone at the center of the skin-to-core interface is based on the FE model that was developed in [28]. Some features of meshing and differences between the two FE models are briefly presented in this subsection.

In Fig. 4a the finite element model of the debonded sandwich plate developed with the ABAQUS code is shown. Reduced integrated 8-node continuum shell finite elements SC8R with displacement degrees of freedom only are used for discretization of the skins. These elements enable to model both thin and thick plate/shell problems. In the case of skins made of laminated composites, the continuum shell elements are stacked to provide a more refined through-the-thickness response.

The core of the sandwich plate is modelled with first-order reduced integrated 8-node continuum solid "brick" elements C3D8R which are directly connected to the continuum shell elements representing the skins. To avoid the hour-glassing problem in these elements, the "hourglass stiffness" method available in ABAQUS is used. More details concerning the finite elements involved can be found in [34].

After preliminary convergence tests concerning the refinement of the FE spatial discretization from a viewpoint of both the solution accuracy and the computational cost, the general mesh of the sandwich plate contained one layer of the continuum shell elements for each skin and ten layers of the brick elements for the core through the plate thickness. The mesh was generated by partition of the total model onto several parts, which are connected with each other through share nodes. The penny-shaped debonded zone was presented by an actual small gap between the finite elements of the upper skin and the core. The mesh density was higher in the central part of the plate, where the contact-impact phenomenon is expected to be modelled and it was rougher for the remaining part of the plate. No artificial adjustment of either the material or geometrical properties was made at the debonded region to ensure as close as possible a physically real case.

The contact surfaces between the skin and the core are formed by faces of the underlying finite elements. Since the surfaces coming into contact have high dissimilar mechanical properties, a pure master-slave contact pair formulation in ABAQUS was applied, Fig. 4b. The small-sliding contact tracking algorithm was utilized for the contacting surfaces because small oscillations are presumed. The "hard" contact model available in the code implying no penetration at each constraint location and no contact pressure transmission unless the surfaces are in contact was accepted to model normal interactions between the contacting surfaces. The isotropic Coulomb friction model specified the contact behavior of these surfaces in tangential directions. Unlike the finite model developed in [28], in the present model, the contact constraints were imposed and the contact forces were calculated by using the penalty contact enforcement method described shortly in Section 2.4. This contact method is consistent with the implicit solver of ABAQUS/Standard, which uses the HHT integration scheme for a general dynamic analysis and the backward difference approach for a friction prediction, [34].

Table 1: Material properties of the foam-cored sandwich plate.

Components	Elastic constants
Foam Core	$E_c = 85$ MPa, $G_c = 30$ MPa, $\rho_c = 52$ kgm^{-3}
Face sheet	$E_{xx} = E_{zz} = 19.3$ GPa, $E_{yy} = 3.48$ GPa, $G_{zx} = 7.7$ GPa, $G_{xy} = G_{yz} = 1.65$ GPa, $\rho = 1650$ kgm^{-3}

3. Numerical results

One configuration of the sandwich plate containing a penny-shaped debonded zone is used throughout numerical predictions in what follows. The rectangular sandwich plate of length $a = 270$ mm and width $b = 180$ mm consisting of a 50 mm-thick WF51 foam core and 2.4 mm-thick GFRP skins is simply supported along all four edges. The radius of central debonded zone is 20 mm. The mechanical properties of constituent materials of the sandwich plate are taken as in [28] and are listed in Table 1.

First, the modal analysis of the debonded sandwich plate is needed for evaluating its natural frequencies. However, this analysis does not take into account contact within the debonded region. To keep the finite element model capacities in modelling the contact and friction phenomena, free decay oscillations of the debonded sandwich plate after an impulse loading are simulated and, then, its natural frequencies are extracted from corresponding transient time signals.

3.1. Impulsive loading

The debonded sandwich plate is subjected to an impulse concentrated force at the central point of its lower undamaged skin. The duration of the applied force is taken much shorter than the analysis time (one tenth of the analysis time step), i.e.

$$F(t) = \begin{cases} F_0, & 0 \le t \le t_* \\ 0, & t > t_* \end{cases}$$

with the amplitude of $F_0 = 10$ kN and the time $t_* = 1$ ms. It should be noted that the force amplitude is chosen so that neither geometrical nor material nonlinearities are activated. For this purpose an overall deflection and stress states within the both skins and the lightweight core of the sandwich plate were examined under the applied force in preliminary studies that are not presented in the current paper, but are the same as in [35].

The dynamic transient analysis accounting for the contact behavior between the detached layers is performed with ABAQUS/Explicit implementing the computational algorithms

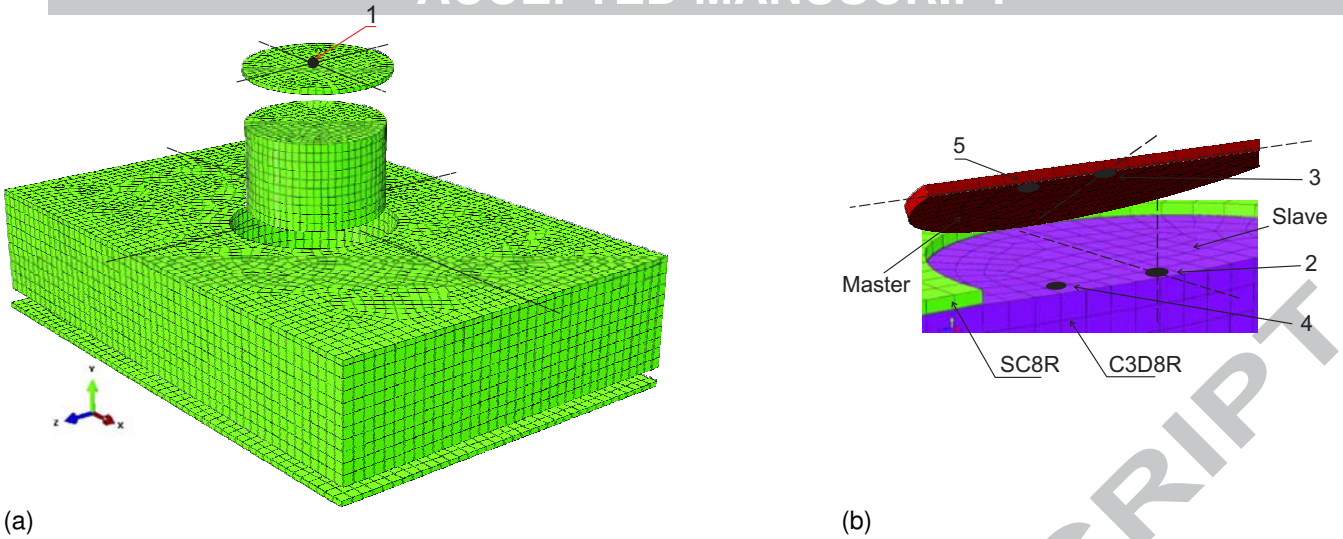

Figure 4: The debonded sandwich plate with penny-shaped debonded zone: a) 3-D FE model; and b) details of modelling at the debonded zone.

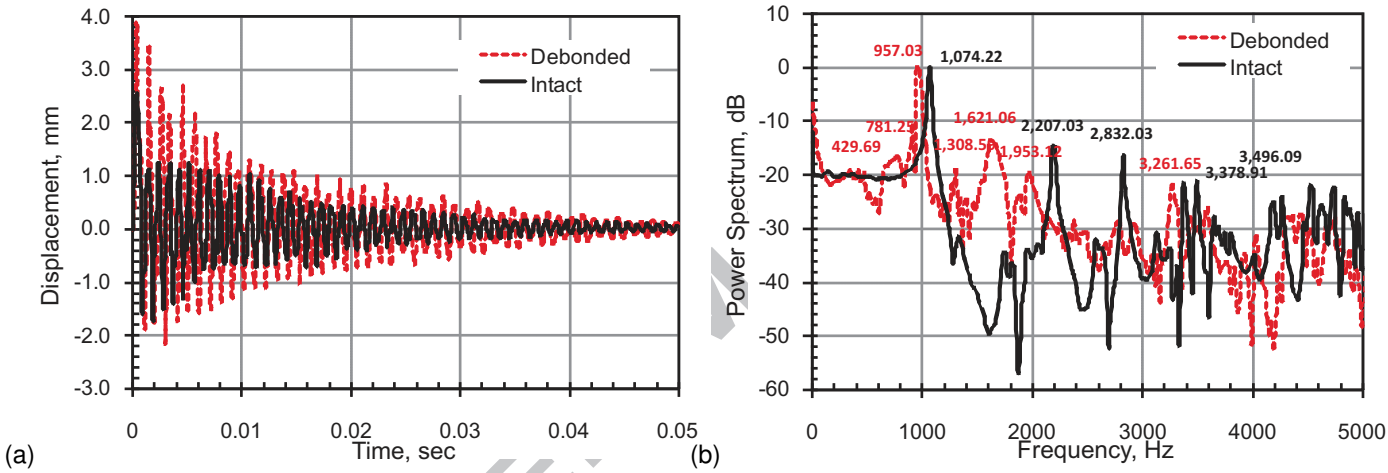

Figure 5: Transient dynamic response of the intact and debonded sandwich plates in: a)time domain; and b) frequency domain.

described in [28]. The transient displacement time signals of the sandwich plates with and without debond are calculated at the central point N 1 (see Fig. 4a) and are displayed in Fig. 5a. One can see that the presence of debond increases the amplitude, but decreases the frequency of free decay vibrations of the sandwich plate. This result is attributed to decreasing the plate stiffness due to the debond existence.

The time histories calculated are processed by using the Fast Fourier Transform (FFT) within the Matlab software environment [36] to convert them into frequency domain data. The comparisons between appropriate power spectra of the debonded and the same intact sandwich plates are shown in Fig. 5b, where only several peaks are signed as examples.

In Table 2, several natural frequencies extracted from the spectral signals of the intact and debonded plates are listed. It follows from Table 2, all the natural frequencies tend to decrease with increasing the number of mode, but this effect does not exhibit a monotonic character. The amount of frequency drop is dependent on the mode of interest, as seen in

Table 2: Natural frequencies (Hz) of the intact sandwich plate and the sandwich plate with the 10%-sized debond.

Intact	Debonded	Intact	Debonded
1074.2	957.03	2832.0	2675.8
1562.5	1308.6	2968.8	2792.9
1757.8	1406.3	3144.5	2910.2
1953.1	1621.1	3261.7	3007.8
2187.5	1953.1	3378.9	3281.3
2285.2	2109.4	3496.1	3359.4
2578.1	2382.8	3750.0	3593.8
2675.8	2500.0	3808.6	3785.1

Fig. 6. More detailed discussions concerning the influence of the debonded zone on natural frequencies and associated mode shapes of sandwich plates can be found in [23, 24].

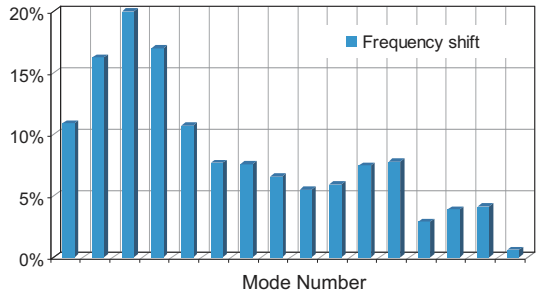

Figure 6: Shift in natural frequencies between the intact and debonded sandwich plates.

One can see from Fig. 5b that the frequency signal of the debonded plate is characterized by wider peaks at the resonance frequencies in comparison with those of the intact plate. This indicates higher material damping in the debonded sandwich plate. Besides, additional peaks both before the fundamental frequency and in the domain of high frequencies can evidently be observed in the frequency content of the debonded plate. This is a result of superimposing between vibration waves caused by the external impulsive load and generated by contact interactions within the debonded region. Thus, the influence of the presence of debond on the dynamic transient response of sandwich plate is significant.

3.2. Harmonic loading

Because long-term dynamical responses are of concern, rather than particular transient events, the harmonically forced vibrations of the debonded sandwich plate are investigated further. The simulations are carried out with finite element model developed in ABAQUS/Standard that incorporates the implicit integration algorithm for a general dynamic analysis with contact described in Section 2. The sandwich plate with the circular debonded zone is excited with a prescribed harmonic transverse displacement $u(t) = u_0 \, sin(\Omega t)$ applied at the central point of lower perfectly attached skin. The dynamic response of the plate is investigated for the fixed excitation amplitude u_0 equal to 5 mm by varying the excitation frequency Ω. Different driving frequencies are investigated. They were selected so that a harmonic load applied could be able to highlight some specific dynamic phenomena occurring in the sandwich plate. For the convenience's sake, the driving frequencies are presented by a fraction of the fundamental frequency of the same intact sandwich plate f_0, i.e. $\eta = \Omega / f_0$.

In simulations, because no experimental data concerning the energy dissipation phenomenon is known in the plate, the artificial viscous damping and friction are included into the model in such a way that the behavior of plate would be simulated to some extent of reality, but without hard numerical difficulties inflicted by these phenomena. In this respect, the modal damping ratio was assumed equal to 1% of the critical value throughout this study, hence, the appropriate damping coefficients of the Rayleigh damping matrix $\mathbf{C}$ in (11) were being calculated for each frequency range of interest. For frictional contact the coefficient of friction was accepted equal to $\mu = 0.1$ that is a lower boundary of the range of friction coefficients for plastic-plastic material combinations.

It is worth to notice that all time history plots, presented below to indicate the degree of repeatability of forced dynamic responses being investigated are calculated for transverse displacements and velocities at the central point N 1 (see Fig. 4a) and at the two points N 2 and N 3 collocated on the contacting surfaces of core and upper skin in the debonded zone (see Fig. 4b). The former representative point is chosen to illustrate the global dynamics of the plate, while the latter points specifying a contact pair are defined to display a complex response of the "breathing" debonded zone in detail. The time signals are shown in a time range, when the steady state motion of a vibrating plate has been achieved. Besides, data computed in each run are stored for a one-tenth part of a current excitation period. In doing so, the data are truncated so that each time history record contains an exact integer number of excitation periods, thus minimizing leakage and avoiding the need to use windows in the FFT. As well, each state space trajectory (or phase portrait) combining displacement and velocity time histories is made up of a time interval, which includes at least of 20 periods of excitation after ceasing the transient motion. And if it is necessary to obtain a deeper insight into the type of motion being considered, those phase space data are stroboscopically sampled every forcing period of excitation to construct Poincaré sections.

The frequency ratio of 1/2 leading to the driving frequency about of 500 Hz is firstly considered for the displacement load. Figs. 7a and d present deflection time histories of the sandwich plates with and without debond at the point N 1 and the detached skin and the remaining part at the points N 2 and N 3 in the debonded plate. Their appropriate phase portraits are presented in Figs. 7b and e, respectively. Analyzing these plots, one can see that a periodic motion with frequency, which is the same as the excitation frequency, without contact between the debonded parts occurs in the debonded sandwich plate. It means that for the given debonded zone size and the excitation level, inertial forces in the plate are too low to overcome the clearance existing between the detached skin and the core, i.e. these parts are not in contact at the central points of the debonded zone. However, very small distortions, visible in the time responses and the phase portraits of the detached skin and remaining plate reflect the existence of a light contact between them. The contact takes place at some points nearby to the boundary of the debonded zone. This fact was visualized by the animation of the deformation time history of plate within the post-processor of the ABAQUS code (not presented here). It was found out that a source of this contact is a rotation of the thinner detached skin. The appearance of additional odd harmonics with small energy contributions in the frequency spectrum of the debonded sandwich plate is an evidence of such light contacts, Figs. 7c and f. A unit decibel (dB) is used to see easily these small signal components in the presence of

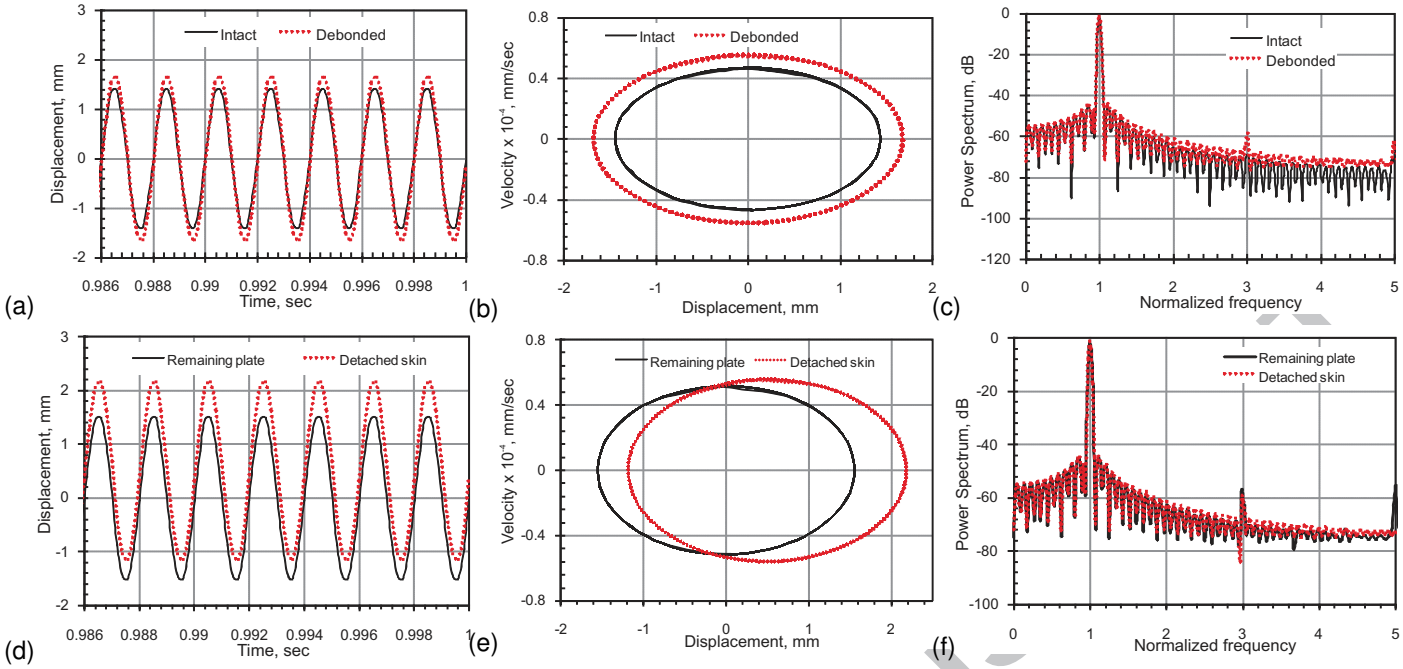

Figure 7: Dynamic response at $\Omega = 500\ Hz$: a) displacement time history, b) phase portrait and c) frequency spectrum of the both debonded and intact plates; d) displacement time history, e) phase portrait and f) frequency spectrum of the detached skin and the remaining plate.

the large component corresponding to the excitation frequency. Thus, as expected, the use of the three-dimensional model allows one to more accurately simulate and more precisely analyze the dynamics of the debonded plate.

At the kept excitation amplitude, the contact behavior between the detached segments of the debonded sandwich plate was noticed for the frequency ratio of 3/4 that corresponds to the driving frequency about of 800 Hz. A comparison of time histories, phase portraits and power spectra of the sandwich plates with and without debond are shown in Figs. 8a-f at the point N 1 and points N 2 and N 3 mentioned earlier. It follows from these plots that the debonded sandwich plate has a periodic motion with one contact at each cycle of the excitation. One can see in Figs. 8a and b that the amplitudes of the debonded plate's histories are larger than those in the time signals of the same intact plate. As well, the amplitude of the detached skin's displacement is larger compared to the amplitude of the remaining plate's displacement, Fig. 8d. In doing so, the both plates as well as the debonded parts oscillate in the same phase, while the waveforms of displacement signals in the debonded plate show an asymmetry associated with "breathing" the debond. As seen in Fig. 8d, the detached parts coming into contact once every excitation period remain in contact relatively long. It means that both impact-like and slipping interactions contribute to the energy loss during contact. Thus, the contact can be thought as a phenomenon in which exists two regimes: the "chattering regime", which is caused by impact-like events, where the detached surfaces bounce off each other with enough energy to hit themselves again and the "normal force controlled regime", where the detached segments lose sufficient energy during the impact to stay in continuous frictional contact, as have been presented in [10, 13] based on oscillator models. Moreover, the periodically colliding detached surfaces produce harmonics that are integer multiple of the forcing frequency, as can be seen in the debonded plate's frequency content in Fig. 8c. Therewith, the detached skin and the remaining plate reveal different energy distributions in their spectral contents, Fig. 8f. The greatest amount of vibrational energy is predominantly localized at the higher frequencies in the frequency spectrum of the remaining plate, while the lower frequencies have the greatest energy in the frequency signal of the detached skin. Seemingly the remaining part comes across the detached skin during oscillations, thereby, it experiences the excitations produced by both the contact interactions and the external load.

When the frequency ratio is increased up to $\eta = 2$, i.e. the driving frequency is about of 2000 Hz, the qualitative character of the debonded plate's response is changed from the previous cases noticeably. In general, as indicated by the displacement time histories, phase portraits and frequency spectra in Fig. 9a-f, the response of the debonded plate is a period-one motion. However, in this case the oscillations of the debonded and intact plates are not coincident in the phase, Fig. 9a. Herewith, the displacement amplitude of the debonded plate and, as a consequence, the amplitude of its velocity exceed those amplitudes of the intact plate in several times. This can clearly be seen by tracking the appropriate phase orbits of the both plates in Fig. 9b. Also, the detached skin and the remaining part oscillate in the anti-phase to each other, as displayed in Fig. 9d. As a result, another type of contact than it was observed earlier takes place between them. One can see from Fig. 9d, although the detached surfaces continue to come into contact once per cycle of the excitation, but now the impact-like contact prevails in

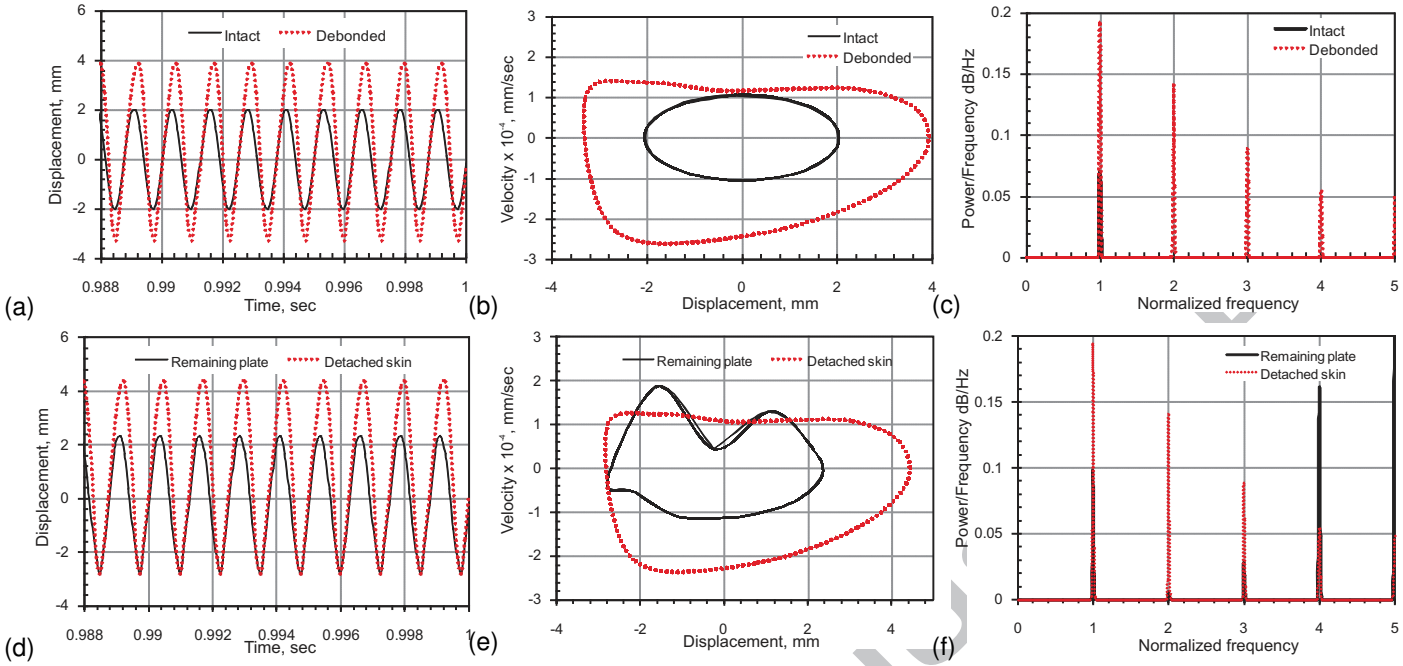

Figure 8: Dynamic response at $\Omega = 800\ Hz$: a) displacement time history, b) phase portrait and c) frequency spectrum of the both debonded and intact plates; d) displacement time history, e) phase portrait and f) frequency spectrum of the detached skin and the remaining plate.

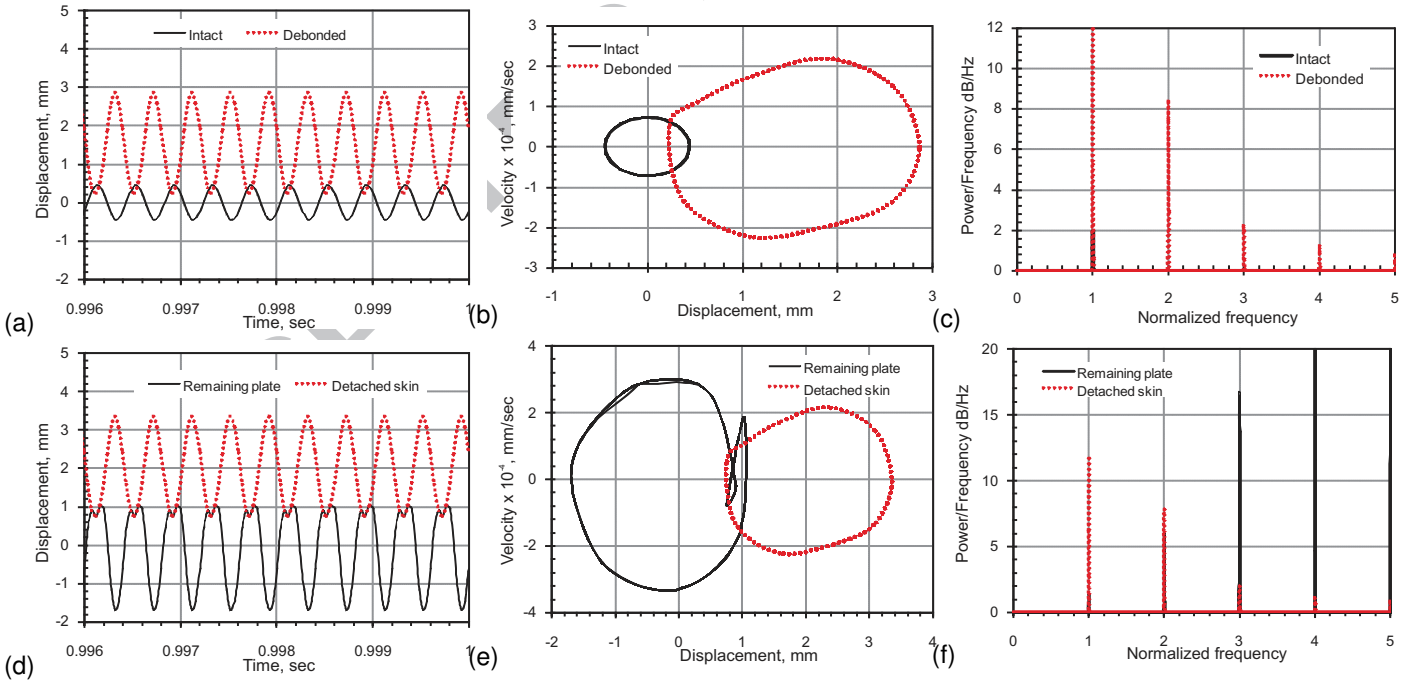

Figure 9: Dynamic response at $\Omega = 2000\ Hz$: a) displacement time history, b) phase portrait and c) frequency spectrum of the both debonded and intact plates; d) displacement time history, e) phase portrait and f) frequency spectrum of the detached skin and the remaining plate.

their interactions. The near-vertical portion of the corresponding phase portrait in Fig. 9e depicts such impact-like contacts. Moreover, both the inward bend in the phase portrait in Fig. 9e and the large amplitudes of high frequencies in the frequency spectrum in Fig. 9f for the remaining part have their sources in those impacts as well.

With further increasing the driving frequency up to $\eta = 3$, i.e. about 3000 Hz, a period-two motion has been detected. It follows from the analysis of graphs in Figs. 10a-f. Figs. 10c and f display that the frequency components in the spectral signals of the debonded plate occur at both the harmonics and exactly half the harmonics of the excitation frequency. It means that new frequencies generated due to contact events in the debonded region are fractional multiple, namely one-second of the forcing frequency. Because of phase-locking the global dynamic response of the debonded plate becomes the period-two motion. Therewith, the displacement amplitude of the debonded plate's signal is larger significantly than that amplitude of the intact plate's signal, as depicted in Fig. 10a. This subharmonic character of the motion is borne out by the two points in the Poincaré section in Fig. 10b, as well. In Fig. 10d the displacement time histories of each debonded part are demonstrated. It is clearly seen that the detached skin and the remaining part come into contact twice per cycle of the excitation. Their state space portraits in Fig. 10e display that such contacts involve both the "chattering regime" and the "normal force control regime". It is worthily for noticing that similar subharmonic motions for a cracked beam predicted using a three-dimensional finite element model was recently reported in [37].

The interesting behavior of the debonded sandwich plate, distinctive from all the cases revealed here is obtained at the frequency ratio $\eta = 4$, i.e. about of 4000 Hz. As shown in Figs. 11a-c, the debonded sandwich plate has a periodic-one motion differing significantly from the harmonic oscillations of the intact plate. One can clearly see that there is a phase shift between the time signals of the both plates. The phase trajectory of the debonded plate is not an ellipse and is markedly larger than that of the intact plate. As well, the frequency spectrum of the debonded plate contains harmonics of the excitation frequency. The reason of this response of the debonded plate was found by tracking the time history displacements and velocities at different points of the debonded zone. It results from Figs. 11d and e, while the debonded parts have lost the contact at the central points N 2 and N 3 during the oscillations, they are in contact at other points. As an example the plate response is presented at the points N 4 and N 5 (see Fig. 4b) that are located about half the debonded zone's radius R from the center. At these points two contacts each excitation cycle take place, Fig. 11e. The contacts are characterized by both impact-like and sliding interactions, as seen in the appropriate phase portraits in Fig. 11f. Therewith, high order frequency components are prevail in the frequency spectrum of the remaining plate as indicated by a lobe on the phase trajectory. This described case confirms again the need of the three-dimensional presentation of the debonded plate's dynamic response to properly model the complex nonlinear behavior.

At the frequency ratio $\eta = 5$ (or about 5000 Hz for the driving frequency), the numerical predictions showed a quasi-periodic dynamics of the debonded sandwich plate. This result follows from the plots in Figs. 12a-f. The frequency spectrum shown in Fig. 12a along with the peaks at the excitation frequency and its harmonics exhibits sidebands consisting of at least two components well visible on the frequency-axis. These frequencies are incommensurate with the excitation frequency. As shown in Fig. 12b, the phase plane contains several forms of the state space trajectories for the debonded plate motion. Moreover, the Poincaré map of the motion in Fig. 12c gives a closed curve. Figs. 12d-f clearly display that there exist different kinds of contact between the detached surfaces of the plate. The contacts repeat at some time interval during the plate oscillations. Within that interval, some of contacts are strongly impact-like that are observed by near vertical portions of the phase orbits, but other ones are with a some extent of sliding, Fig. 12e. As a result of such almost regular contacts within the debonded zone, newly created frequencies are incommensurate with the excitation frequency that result in the global quasi-periodic motion observed in this case.

The last predictions were carried out at the frequency ratio of 7, that leads to the driving frequency about of 7000 Hz. Data computed for this case are presented in Figs. 13a-f. Unlike the intact plate the evolution with time of the deflection of debonded plate is not regular, as given in Fig. 13a. Moreover, the state space trajectory of the debonded plate in the phase plane does not repeat itself ever again for excitation periods, Fig. 13b. A set of points in the Poincaré section in Fig. 13c corresponds to irregular variations of the motion from one excitation cycle to another one. From the frequency response curve in Fig. 13d one can see that the spectral spikes, which are evident in the response spectrum, are surrounded by a distribution of frequencies having the character of a broadband, i.e. some amount of the vibrational energy is localized within the band around. Successive impacts between the remaining plate part and the detached skin are not regular in accordance with plots presented by their phase orbits and Poincaré sections in Figs. 13e and f, respectively. Thereby, the oscillations of the debonded plate at the given driving frequency looks like a chaotic motion. To verify this assumption, the largest Lyapunov exponent was calculated for the space trajectory of debonded plate using the methodology proposed by Rosenstein et al. within the TISEAN package [38]. In assumed chaotic regime the dominating Lyapunov exponent had a statistically significant value of about 0.16. This positive Lyapunov exponent clearly indicates the chaotic behavior in the debonded sandwich plate.

4. Conclusions

Dynamics of the debonded foam-cored sandwich plate subjected to both impulse and harmonic loads is studied using the finite element analysis with taking into account intermittent contact between the detached segments within the damaged skin-to-core interface. The finite element model proposed revealed a wide range of behaviors appearing in the debonded sandwich plate being simulated. The numerical results showed

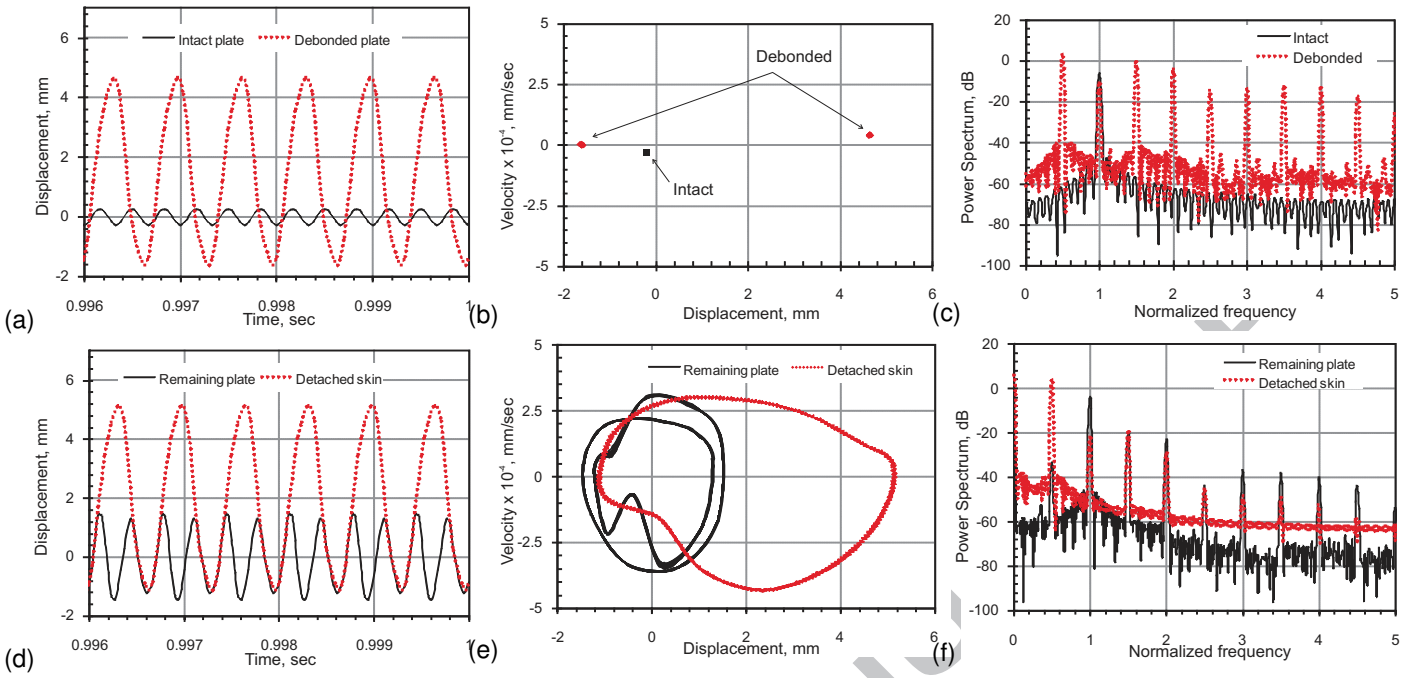

Figure 10: Dynamic response at $\Omega = 3000\ Hz$: a) displacement time history, b) Poincaré section and c) frequency content of the both debonded and intact plates; d) displacement time history, e) phase portrait and f)frequency content of the detached skin and the remaining plate.

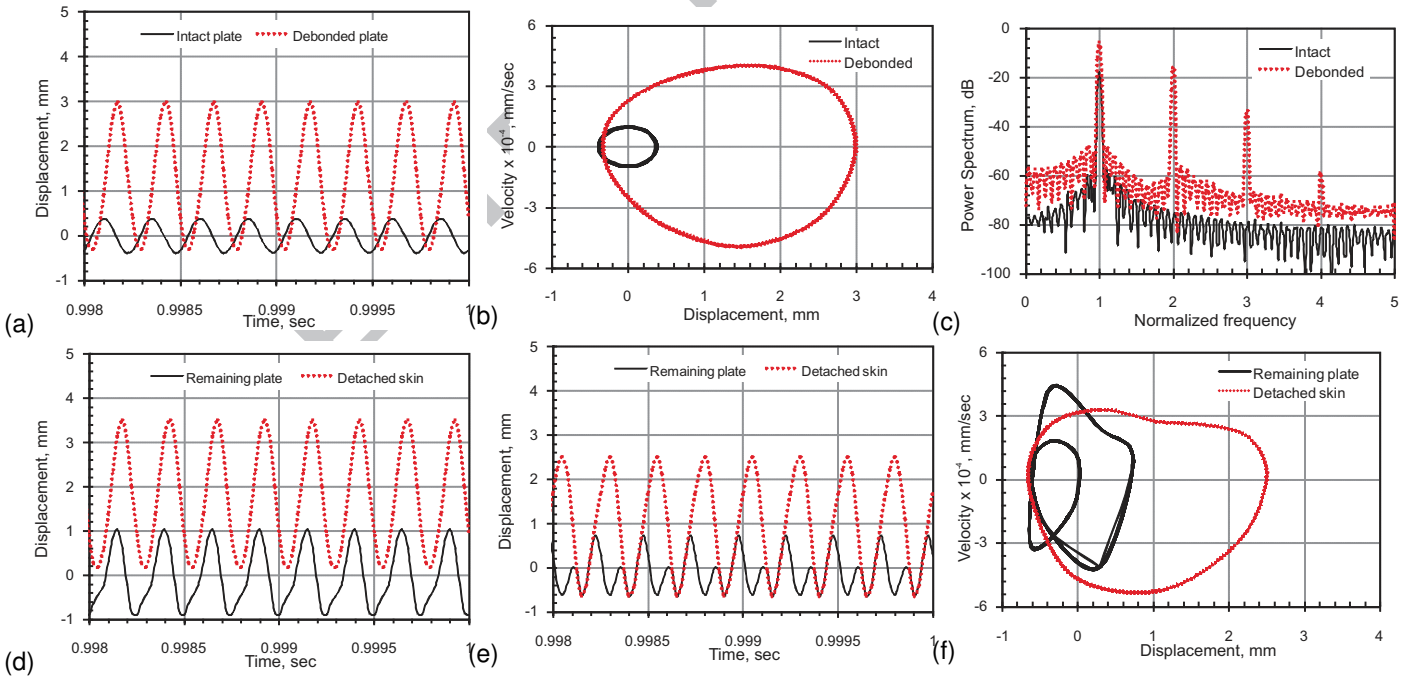

Figure 11: Dynamic response at $\Omega = 4000\ Hz$: a) displacement time history, b) phase portrait and c) frequency content of the both debonded and intact plates; d) displacement time history at the points N 2 and N 3, e) displacement time history at the points N 4 and N 5 and f) frequency content of the detached skin and the remaining plate.

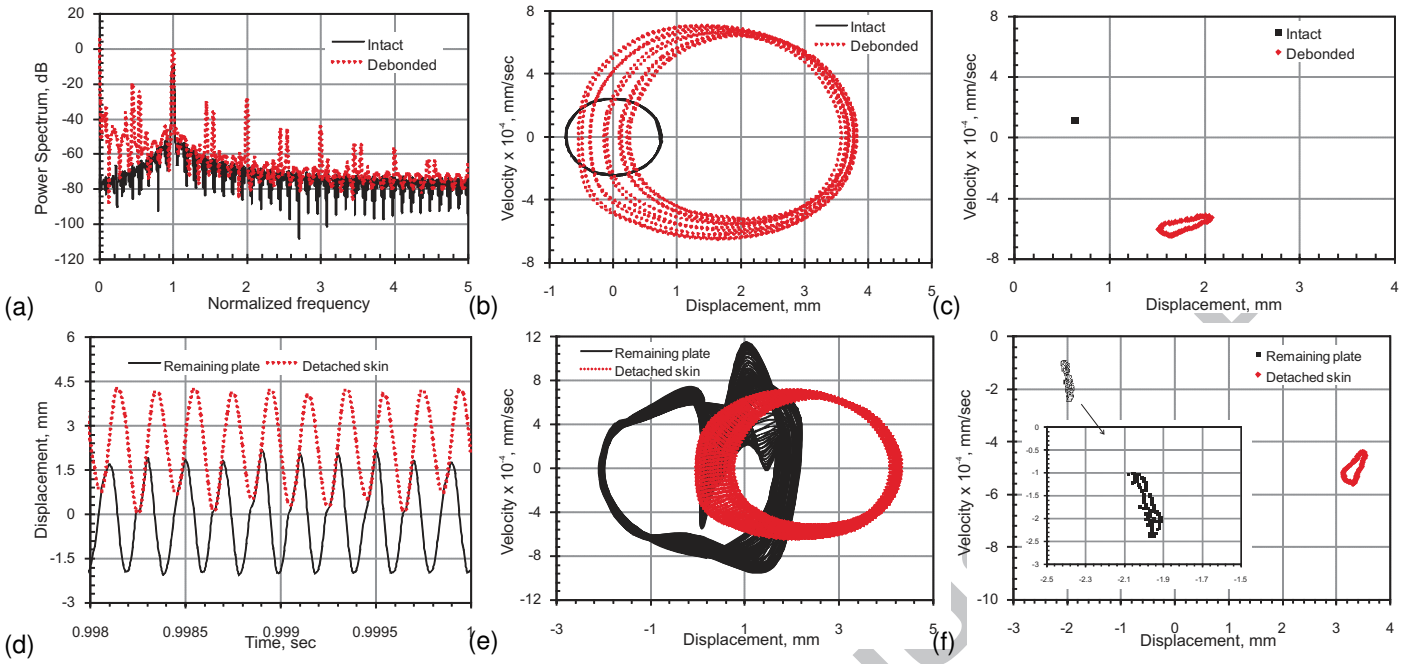

Figure 12: Dynamic response at $\Omega = 5000\ Hz$: a) frequency content, b) phase portrait and c) Poincaré section of the both debonded and intact plates; d) displacement time history, e) phase portrait and f) Poincaré section of the detached skin and the remaining plate.

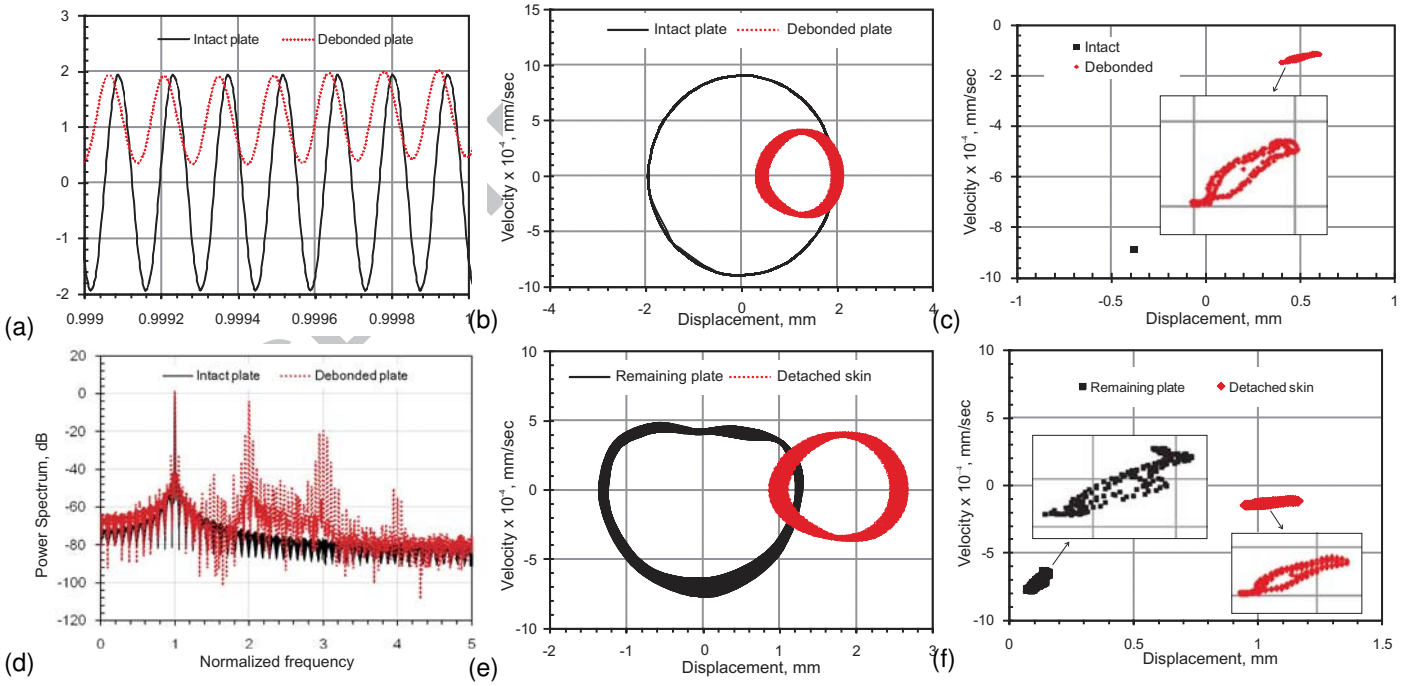

Figure 13: Dynamic response at $\Omega = 6000\ Hz$: a) frequency content, b) phase portrait and c) Poincaré section of the both debonded and intact plates; d) displacement time history, e) phase portrait and f) Poincaré section of the detached skin and the remaining plate.

that both an impulse response and a steady-state response of the debonded sandwich plate is considerably affected by the debond. It was found out that contacts arising within the debonded zone are responsible for the extent of nonlinearity of the plate's structural responses observed. As a result of those contacts, the frequency spectra of the both transient and steady-state vibrations revealed additional frequency peaks in the frequency domain. A redistribution of the vibrational energy to the sub- and super-harmonics seems the main signature of the forced dynamics of debonded plates.

Moreover, the typical assumption that if excitations are harmonic, then the response is also harmonic, commonly used in linear system is no longer valid for the dynamic response of the debonded sandwich plate. Instead, a steady-state response of such systems should be studied based on the general dynamic analysis with a periodic loading function. The driving frequency was considered as a dominant factor that governs by the dynamics of the debonded plate subjected to harmonic loading. The numerical predictions were carried out at the excitation frequencies between one-half and seven times of the fundamental frequency. Within the mentioned frequency interval, numerically predicted behaviors of the debonded plate encompassed a wide range of motions such as harmonic with the frequency equal to the excitation frequency, periodic with period-one and period-two, quasi-harmonic, and chaotic. Super-harmonics were always observed in the frequency spectrum of the debonded plate, sometimes they were even the strongest harmonics in the spectrum. The appearance of period-two, quasi-harmonic, chaotic motions is explained as a result of the intermittent contact between the detached segments that enables to produce new frequencies. The newly created frequencies could be either commensurate or incommensurate with the excitation frequency. Phase plains and Poincaré sections obtained from the numerical predictions were used to analyze those system dynamic behaviors. One can notice that the FE model proposed here can be used as a useful research tool for investigations of a non-linear dynamics of sandwich plates including aspects of damage identification.

Acknowledgement

The research leading to these results has received funding from the European Union Seventh Framework Programme (FP7/2007-2013), FP7-REGPOT-2009-1, under grant agreement No. 245479.

References

[1] J.R. Vinson, Plate and Panel Structures of Isotropic, Composite and Piezoelectric Materials, Including Sandwich Construction, Springer, 2005.

[2] L.A. Carlsson, G.A. Kardomateas, Structural and Failure Mechanics of Sandwich Composites, Springer Science+Business Media B.V., 2011.

[3] J. Hohe, L. Librescu, Recent results on the effect of the transverse core compressibility on the static and dynamic response of sandwich structures, Compos. Part B 39(1) (2008) 108–119.

[4] E. Carrera, S. Brischetto, A survey with numerical assessment of classical and refined theories for the analysis of sandwich plates, Appl. Mech. Rev. 62(1) (2009) 1–17.

[5] D. Elmalich, O. Rabinovitch, A high-order finite element for dynamic analysis of soft-core sandwich plates, J. Sandwich Struct. Mater. 14(5) (2012) 525–555.

[6] V.I. Babitsky, Theory of Vibro-Impact Systems and Applications, Springer, Berlin, 1998.

[7] M. Chati, R. Rand, S. Mukherjee, Modal analysis of a cracked beam, J. Sound Vib. 207(2) (1997) 249–270.

[8] V.V. Matveev, A.P. Bovsunovskii, Some aspects of vibration of an elastic body with a "breathing" discontinuity of material, Strength Mater. 32(5) (2000) 434–445.

[9] P. Vielsack, A vibro-impacting model for the detection of delamination, J. Sound Vib. 253(2) (2002) 347–358.

[10] I. Müller, Clapping in delaminated sandwich-beams due to forced oscillations, Comput. Mechanics 39(2) (2007) 113–126.

[11] G. Luo, X. Lv, Dynamics of a plastic-impact system with oscillatory and progressive motions Int. J. Non-Linear Mech. 43 (2008) 100–110.

[12] G. Lancioni, S. Lenci, U. Galvanetto, Non-linear dynamics of a mechanical system with a frictional unilateral constraint, Int. J. Non-Linear Mech. 44(6) (2009) 658–674.

[13] O.K. Ajibose, M. Wiercigroch, E. Pavlovskaia, A.R. Akisanya, Global and local dynamics of drifting oscillator for different contact force models, Int. J. Non-Linear Mech. 45(9) (2010) 850–858.

[14] Q. Li, Y. Chen, Y. Wei, Q. Lu, The analysis of the spectrum of Lyapunov exponents in a two-degree-of-freedom vibro-impact system, Int. J. Non-Linear Mech. 46 (2011) 197–203.

[15] C.N. Della, D. Shu, Vibration of delaminated composite laminates: a review, Appl. Mech. Rev. 60 (2007) 1–20.

[16] J.S. Hu, Ch. Hwu, Free vibration of delaminated composite sandwich beams, AIAA J. 33(10) (1995) 1911–1918.

[17] Y.Y. Wang, K.Y. Lam, G.R. Liu, Detection of flaws in sandwich plates, Compos. Struct. 34 (1996) 409-418.

[18] H.-Y. Kim, W. Hwang, Effect of debonding on natural frequencies and frequency response functions on honeycomb sandwich beams, Compos. Struct. 55 (2002) 51-62.

[19] B. Saraswathy, L. Mangal, R. R. Kumar, Analytical approach for modal characteristics of honeycomb sandwich beams with multiple debond, J. Sandwich Struc. Mater. 14(1) (2011) 35-54.

[20] H. Schwarts-Givli, O. Rabinovitch, Y. Frostig, High-order nonlinear contact effects in the dynamic behavior of delaminated sandwich panels with a flexible core, Int. J. Solids Struct. 44 (2007) 77–99.

[21] K.M. Liew, C.S. Lim, Analysis of dynamic responses of delaminated honeycomb panels, Compos. Struct. 39 (1997) 111-121.

[22] A. Chakrabarti, A.H. Sheikh, Vibration and Buckling of Sandwich Laminates having Interfacial Imperfections, J. Sandwich Struct. Mater. 11 (2009) 313-328.

[23] V.N. Burlayenko, T. Sadowski, Influence of skin/core debonding on free vibration behavior of foam and honeycomb cored sandwich plates, Int. J. Non-Linear Mech. 45(10) (2010) 959–968.

[24] V.N. Burlayenko, T. Sadowski, Dynamic behaviour of sandwich plates containing single/multiple debonding, Comput. Mater. Sci. 50 (2011) 1263-1268.

[25] Y.W. Kwon, D.L. Lannamann, Dynamic numerical modeling and simulation of interfacial cracks in sandwich structures for damage detection, J. Sandwich Struct. Mater. 4 (2002) 175–199.

[26] I. Müller, A. Konyukhov, P. Vielsack, K. Schweizerhof, Parameter estimation for finite element analyses of stationary oscillations of a vibro-impacting system, Eng. Struct. 27 (2005) 191–201.

[27] V.N. Burlayenko, T. Sadowski, A numerical study of the dynamic response of sandwich plates initially damaged by low velocity impact, Comput. Mater. Sci. 52(1) (2012) 212–216.

[28] V.N. Burlayenko, T. Sadowski, Finite element nonlinear dynamic analysis of sandwich plates with partially detached facesheet and core, Finite Elem. Anal. Des. 62 (2012) 49–64.

[29] P. Wriggers, Computational Contact Mechanics, second ed., Springer-Verlag, Berlin, 2006.

[30] T.A. Laursen, Computational contact and impact mechanics: fundamentals of modeling interfacial phenomena in nonlinear finite element analysis, Springer-Verlag, 2002.

[31] T. Belytschko, W.K. Liu, B. Moran, Nonlinear Finite Elements for Continua and Structures, John Wiley and Sons, 2002.

[32] H.M. Hilber, T.J.R. Hughes, R.L. Taylor, Improved numerical dissipation

for time integration algorithms in structural dynamics, Earthquake Eng. Struct. Dynamics 5 (1977) 283-292.

[33] A. Czekanski, N. El-Abbasi, S.A. Mequid, Optimal time integration parameters for elastodynamic contact problems, Commun. Numer. Meth. Engng. 17 (2001) 379–384.

[34] ABAQUS User Manual Ver 6.9EF-1, Dassault Systèmes Simulia Corp., Providence, RI, 2009.

[35] V.N. Burlayenko , T. Sadowski, Dynamic Analysis of Debonded Sandwich Plates with Flexible Core Numerical Aspects and Simulation, Advanced Structured Materials 15 (2011) 415–440.

[36] MATLAB 7.9, The MathWorks Inc., Natick, MA, 2009.

[37] U. Andreaus, P. Baragatti, Cracked beam indefication by numerically analysing the nonlinear behaviour of the harmonically forced response, J. Sound Vib. 330 (2011) 721–742.

[38] R. Hegger, H. Kantz, T. Schreiber, Practical implementation of nonlinear time series methods: The TISEAN package, CHAOS 9 (1999) 413–440.